iScience

CellPress
OPEN ACCESS

Article

Engineering bandgap of $CsPbI_3$ over 1.7 eV with enhanced stability and transport properties

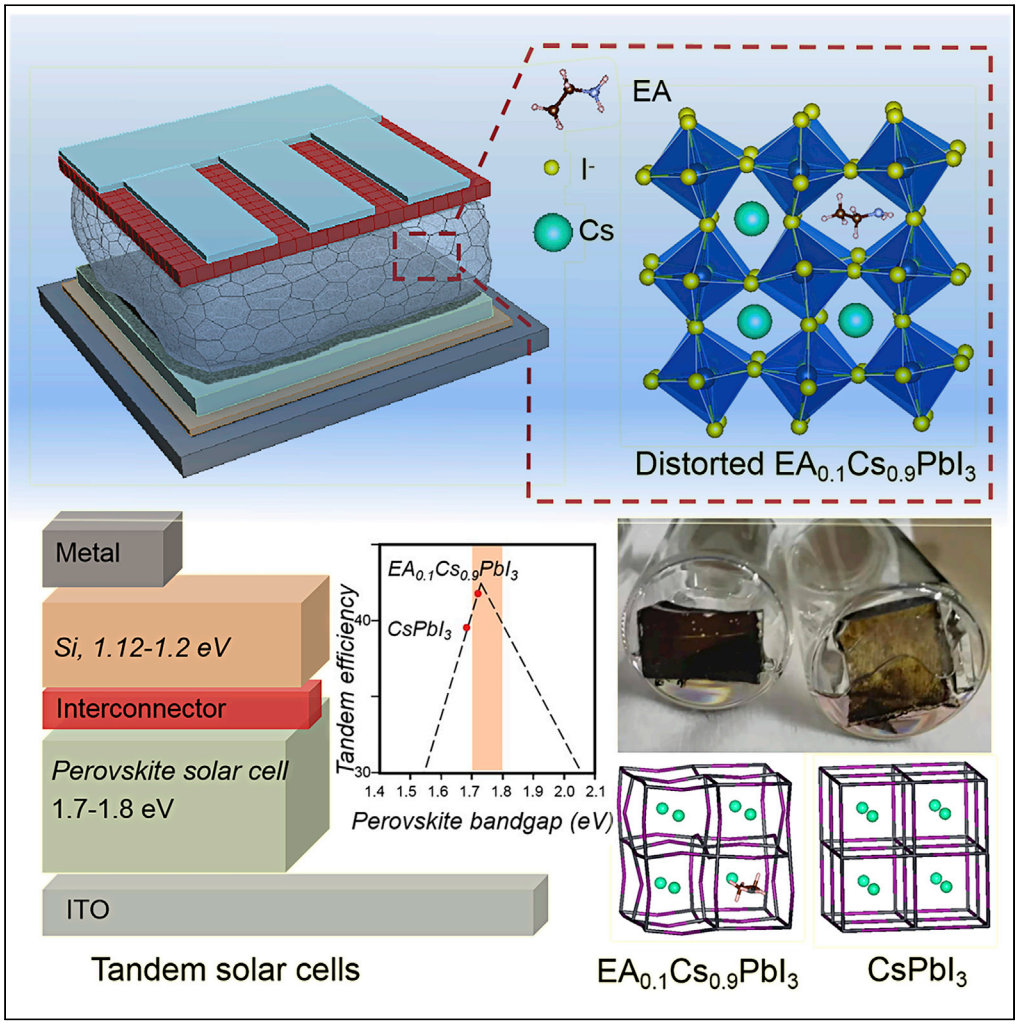

Shumao Xu, Alberto Libanori, Gan Luo, Jun Chen

jun.chen@ucla.edu

HIGHLIGHTS

Perspectives of applying structural distortion to improve the band gap

Perovskites with high band gap over 1.7 eV for potential multijunction application

Enhancing phase stability and transport property without instinct phase separation

The introduction of organic cation of EA with the optimum amount below 0.15

Xu et al., iScience *24*, 102235
March 19, 2021 © 2021 The Author(s).
https://doi.org/10.1016/j.isci.2021.102235

iScience

CellPress
OPEN ACCESS

Article

Engineering bandgap of $CsPbI_3$ over 1.7 eV with enhanced stability and transport properties

Shumao Xu,[1,2] Alberto Libanori,[1] Gan Luo,[2] and Jun Chen[1,3,*]

SUMMARY

Potential multijunction application of $CsPbI_3$ perovskite with silicon solar cells to reach efficiencies beyond the Shockley-Queisser limit motivates tremendous efforts to improve its phase stability and further enlarge its band gap between 1.7 and 1.8 eV. Current strategies to increase band gap via conventional mixed halide engineering are accompanied by detrimental phase segregation under illumination. Here, ethylammonium (EA) in a relatively small fraction ($x < 0.15$) is first investigated to fit into three-dimensional $CsPbI_3$ framework to form pure-phase hybrid perovskites with enlarged band gap over 1.7 eV. The increase of band gap is closely associated with the distortion of Pb-I octahedra and the variation of the average Pb-I-Pb angle. Meanwhile, the introduction of EA can retard the crystallization of perovskite and tune the perovskite structure with enhanced phase stability and transport properties.

INTRODUCTION

Generating electricity from solar radiation is a compelling pathway that could lead to a sustainable energy future for the world (Chen, et al., 2016; Zhang et al., 2016; Zheng et al., 2015; Zhang, et al., 2020; Chen, et al., 2017). Inorganic $CsPbI_3$ perovskite has triggered worldwide interest owing to its relatively large band gap of 1.68 eV to potentially serve as the top cell in tandem devices with silicon solar cell (Yu et al., 2016) and rapid improvement in power conversion efficiency (PCE) from the initial PCE of 0.09% in 2013 to 19.03% in 2019 (Stoumpos et al., 2013; Wang et al., 2019a, 2019b). Despite these clear advantages, cubic black $CsPbI_3$ is unstable at room temperature and tends to transform into the orthorhombic yellow (δ) phase without photovoltaic activity (Straus et al., 2020; Marronnier et al., 2018), largely hampering its further commercialization. Several strategies have been extensively developed to improve the phase stability of $CsPbI_3$ including composition engineering (Tian et al., 2020; Lau et al., 2019; Lu et al., 2020), crystallization regulation by introducing Lewis acid-base adducts (Li et al., 2020a; Nenon et al., 2018) or polymers (Li et al., 2018a; Jeong et al., 2020; Chen et al., 2019) into the $CsPbI_3$ precursor, surface capping treatments (Wu et al., 2019; Wang et al., 2018), and dimension reduction by scaling down to quantum dots (Bai et al., 2019; Sadeghi et al., 2020), nanocrystals (Ghosh et al., 2018), or quasi two-dimensional (2D) films (Qing et al., 2019; Zhang et al., 2017; Mauck and Tisdale, 2019; Liu et al., 2018). Among them, composition engineering by partly replacing Cs^+ with large organic cations can regulate the structural tolerance factor to improve the intrinsic phase stability of $CsPbI_3$ (Xu et al., 2017, 2019; Lee et al., 2021). The soft lattice of $CsPbI_3$ induced by its ionic bonding is favorable for a facile cation exchange to regulate the perovskite composition (Deng et al., 2019). Meanwhile, compared with reducing dimension of perovskites exhibiting insufficient charge transport properties (Wheeler et al., 2018; Li et al., 2020b), alloying organic cations is favorable for the formation of sufficient photocarriers to improve the transport properties in photovoltaic devices (Egger et al., 2020). Therefore, composition regulation to form hybrid perovskites is an ideal strategy for structure engineering to adjust the photoelectric properties. However, engineering $CsPbI_3$ perovskite with organic cations to improve its intrinsic stability is limited to only a few organic cations such as formamidinium (FA) (Hazarika et al., 2018) and methylammonium (MA) (Wang and Chen, 2016). MA and FA cations are inherently unstable in thermal and UV conditions, leading to the degradation of perovskite and the poor lifetime of the photovoltaic devices (Chen et al., 2020b; Juarez-Perez et al., 2016; Yang et al., 2019).

Theoretically, a perovskite-silicon tandem solar cell composed of a silicon bottom cell with a band gap of 1.12–~1.2 eV and a perovskite top solar cell with a band gap of 1.7–1.8 eV can achieve a potential PCE over

[1]Department of Bioengineering, University of California, Los Angeles, Los Angeles, CA 90095, USA

[2]School of Environmental Science and Engineering, Shanghai Jiao Tong University, Shanghai 200240, China

[3]Lead contact

*Correspondence: jun.chen@ucla.edu

https://doi.org/10.1016/j.isci.2021.102235

32% (Yang et al., 2018; Wang et al., 2019c). To date, tremendous efforts have been devoted to the development of high-band-gap (>1.7 eV) perovskites for tandem solar cells based on mixed halide perovskites. However, the development of mixed halide perovskites with a high band gap is shadowed by its light-induced phase segregation (Hoke et al., 2015; Beal et al., 2020). Although several strategies such as tuning interfacial energy level (Tian et al., 2019; Zhang et al., 2019), lowering electron-phonon coupling to reduce the lattice strain (Bischak et al., 2017), and switching from solution process to a full evaporation fabrication (Longo et al., 2017) have been developed to hinder the phase segregation, this detrimental side effect cannot be eliminated inherently. Exploration of new composition engineering methods to form pure-phase high-band-gap perovskites over 1.7 eV with superior stability and transport properties is crucial for perovskite-based tandem solar cells to attain efficiencies beyond the Shockley-Queisser limit.

Here, we investigated ethylammonium (EA^+) as an alternative cation to fabricate a mixed-cation $EA_xCs_{1-x}PbI_3$ perovskite. A small fraction of EA ($x < 0.15$) can be incorporated into the $CsPbI_3$ perovskite framework to form pure-phase hybrid perovskites with enhanced transport properties. The EA incorporation into $CsPbI_3$ would result in a slight increase of the band gap over 1.7 eV originating from the decrease of the average Pb-I-Pb angle. These are quite different from FA incorporation with reduced band gap mainly originating from the decrease of energy states in the conduction band bottom (Yi et al., 2016). This approach of alloying large organic EA cations into $CsPbI_3$ perovskite opens up a new avenue to tune the structures of $CsPbI_3$ perovskite with enhanced phase stability and transport properties for potential multijunction applications.

RESULTS AND DISCUSSION

Structure engineering

A prerequisite for a stable three-dimensional (3D) cubic perovskite structure is having a suitable tolerance factor, *t*, value ranging from 0.8 to 1.0. The *t* value is defined by the equation $t = (r_A + r_X)/\sqrt{2}(r_M + r_X)$, where r_A, r_M, and r_X represent the ionic sizes of a univalent cation, an octahedrally coordinated bivalent metal ion, and a halide ion, respectively (Miyazawa et al., 2018). The *t* value should be close to 1 for a high-symmetry cubic structure. Owing to the small radius of Cs cation (1.67 Å), the tolerance factor of $CsPbI_3$ is only 0.81, which results in the low phase stability of $CsPbI_3$ at room temperature (Xu et al., 2017). Considering the large size of EA^+ (2.3 Å) (Hsu et al., 2015), substitution of Cs with EA causes lattice dilation, which could balance the lattice contraction originating from the small radius of Cs to generate a stable PbI_6 octahedral framework (Figures 1A–1C and see Figure S1). Moreover, introducing a certain amount of EA can interact with I by Lewis base N…I or N-H…I hydrogen bonding (Binek et al., 2015), which can inhibit the phase degradation from halide migration (Lin et al., 2020). With the increase of EA fractions from 0.1 to 0.3, distinct structure distortion with a decrease of the average Pb-I-Pb angle can be observed in $EA_{0.3}Cs_{0.7}PbI_3$ (Figure 1C). Theoretically, the decrease of the average Pb-I-Pb angle with a corresponding variation of the Pb-s/p and I-p antibonding overlap will change the band gap of the hybrid perovskite. The band gap variation upon mixing will be further discussed by band structure calculation. The thermal stability of the perovskite upon mixing can be simulated by dynamic calculation as shown in the bottom row of Figures 1A–1C. $CsPbI_3$ at 500 K exhibits low symmetry structure with distinct tilting of the PbI_6 octahedra. The Pb-I distance in $EA_{0.1}Cs_{0.9}PbI_3$ is longer than that in $CsPbI_3$ at 500 K. The structure of $EA_{0.1}Cs_{0.9}PbI_3$ can be retained at 500 K, whereas the structure of $EA_{0.3}Cs_{0.7}PbI_3$ collapses completely under the same conditions. These simulation results reveal the deteriorated thermal stability upon EA incorporation. In experiment, when heating at 210°C, it took ~10 min for pure $CsPbI_3$ black film to completely turn yellow, whereas this change for $EA_{0.1}Cs_{0.9}PbI_3$ and $EA_{0.3}Cs_{0.7}PbI_3$ took ~7 min and ~3 min, respectively, indicating poor thermal stability in $EA_xCs_{1-x}PbI_3$ hybrid perovskites. The relatively poor thermal stability of organic-inorganic perovskite is mainly induced by the configuration-increased entropy and protons-induced side reactions (Aristidou et al., 2015; Ripalda et al., 2020). After exposing chlorobenzene-submersed films to light, the degradation of $EA_{0.1}Cs_{0.9}PbI_3$ and $EA_{0.3}Cs_{0.7}PbI_3$ films (Figures 1D and 1E) with I_2 release was slower than that of $CsPbI_3$ film (Figure 1F), indicating better structural stability upon EA incorporation. The inhibition of I_2 release during light soaking might be induced by strain engineering (Li et al., 2018b) and enhanced N-I interaction upon introducing large-sized EA (Figures 1B and 1C). Alloying EA^+ in $CsPbI_3$ to form hybrid perovskites with EA fractions between 0.1 and 0.5 can regulate the tolerance factor of $EA_xCs_{1-x}PbI_3$ ranging from 0.82 to 0.87 (Figure 1G).

The transport properties and the energy band structure of pure $CsPbI_3$ and $EA_{0.1}Cs_{0.9}PbI_3$ perovskites were explored by the calculated partial density of states (PDOS) (Figures 1H and 1I). The transport properties of

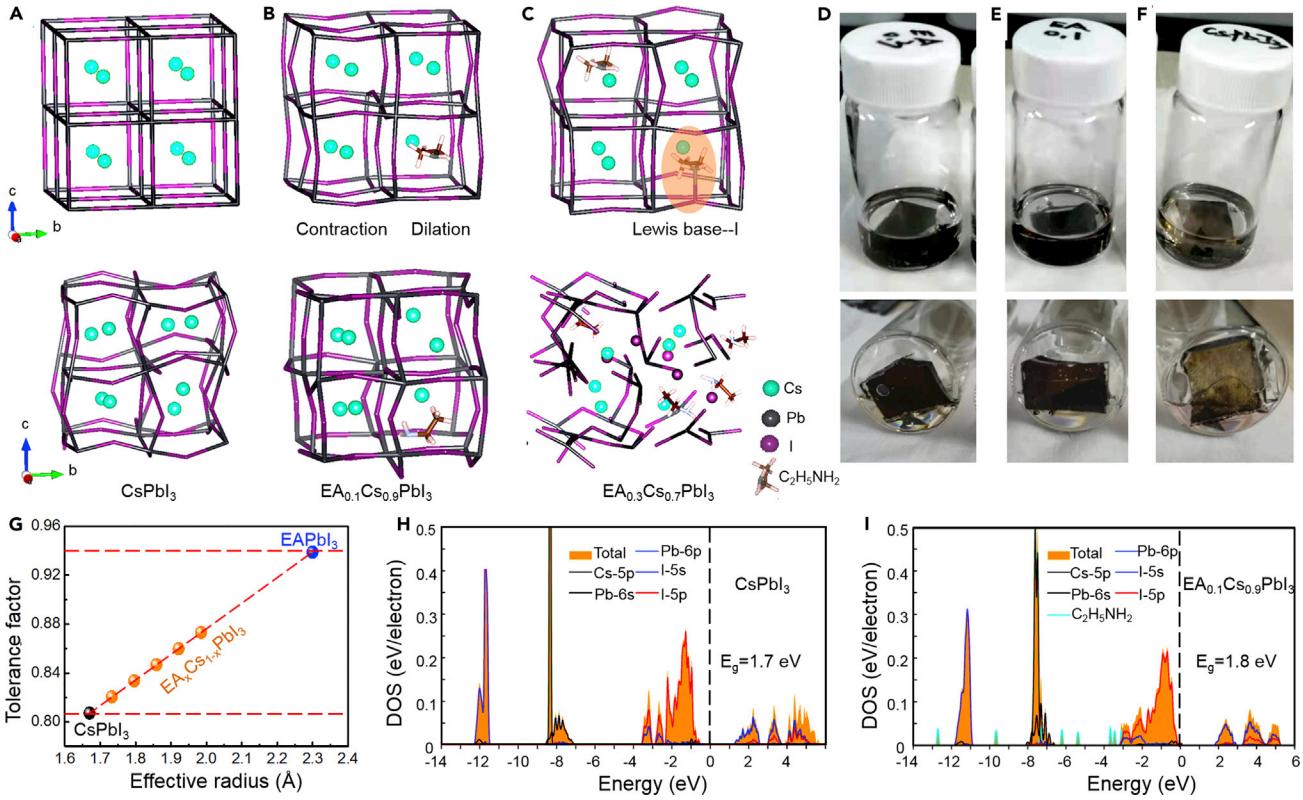

Figure 1. Structure engineering

(A–C) Crystal structure of $CsPbI_3$ (A), $EA_{0.1}Cs_{0.9}PbI_3$ (B), and $EA_{0.3}Cs_{0.7}PbI_3$ (C) at 0 K (top row) and 500 K (bottom row).

(D–F) Photographs of the sealed vials with $EA_{0.3}Cs_{0.7}PbI_3$ (D), $EA_{0.1}Cs_{0.9}PbI_3$ (E), and $CsPbI_3$ (F) after 18 h of light soaking in chlorobenzene under ~2 suns at 19°C.

(G) Tolerance factors of the $EA_xCs_{1-x}PbI_3$ perovskites.

(H and I) Density of states of $CsPbI_3$ (H) and $EA_{0.1}Cs_{0.9}PbI_3$ (I).

the perovskite solar cells mainly refer to the intrinsic electron transport properties from ion migration/accumulation, the light-induced charge carrier numbers, and the charge carrier recombination lifetime. The conduction bands of pure $CsPbI_3$ were mainly composed of Pb 6p, whereas the valence bands were mainly composed of I 5p (Figure 1H). The negligible density of state (DOS) at the Fermi level of $CsPbI_3$ indicated its relatively poor electron transport property. When incorporating EA, the Fermi energy level moved down to the valence band maximum (VBM), indicating a p-type doping property of EA incorporation (Figure 1I). The band gap of $EA_{0.1}Cs_{0.9}PbI_3$ was 1.8 eV, slightly larger than that of $CsPbI_3$, resulting from the increase of the antibonding interaction between I-5p and Pb-6p orbitals. Meanwhile, the incorporation of EA with lattice expansion increases the DOS at the Fermi level suggesting enhanced electron transport properties. EA incorporation contributes mainly to the DOS in the region below the VBM instead of the band gap beneficial for more carriers hopping without trap state recombination (Figure 1I).

Structural characterizations

Figure 2A shows photographs of the $EA_xCs_{1-x}PbI_3$ ($0 \leq x \leq 0.5$) perovskite thin films prepared with different colors. The $CsPbI_3$ inorganic perovskite films with alloyed EA fractions below 0.3 are black purple. The film gradually changed to black brown as the EA concentration increased over 0.3. Further observation by scanning electron microscopy (SEM) revealed the differences in the film morphologies upon introducing different fractions of EA in the films (Figures 2B–2D and see Figure S2). The pure $CsPbI_3$ perovskite film consisted of closely packed crystals with size 300–400 nm (Figure 2B). The $CsPbI_3$ films with EA fractions 0.05 and 0.1 showed a relatively uniform surface with few pinholes, similar to the pure $CsPbI_3$ film. In the $EA_xCs_{1-x}PbI_3$ (x = 0.3, 0.4 and 0.5) samples, the perovskite films are coarse with a noticeable number of pinholes. The thickness of $EA_{0.1}Cs_{0.9}PbI_3$ film was ~520 nm (Figure 2C). As shown in Figure 2E, the main

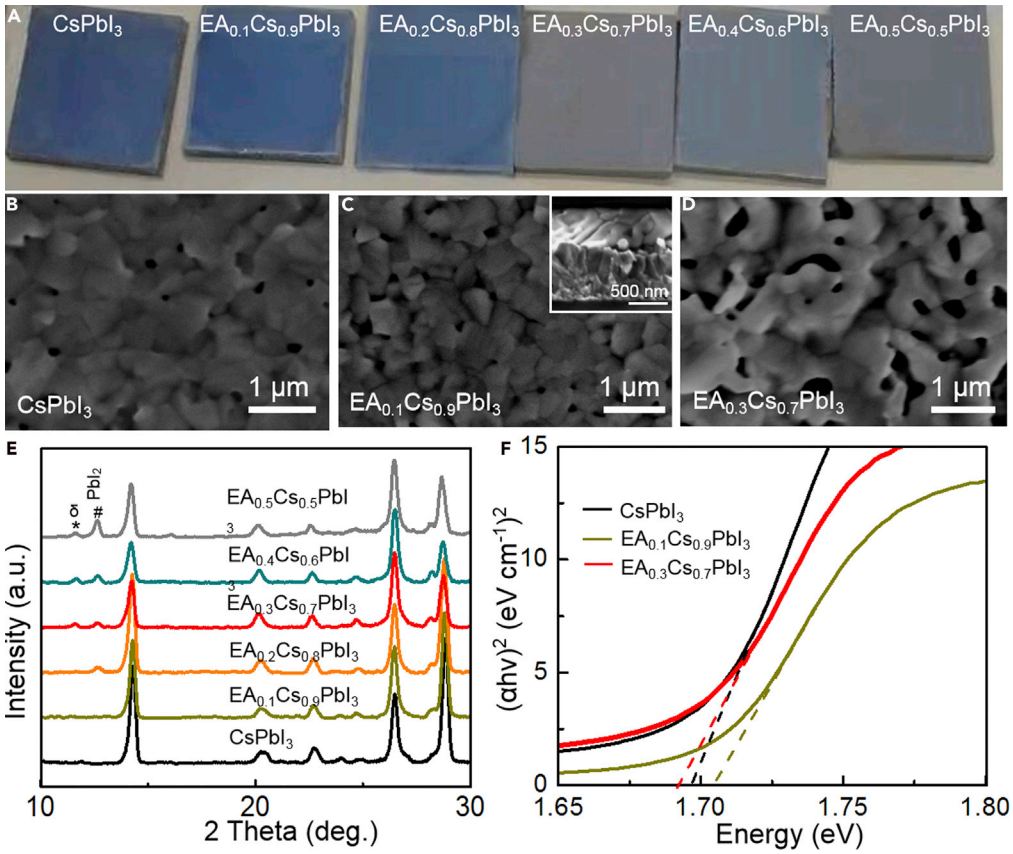

Figure 2. Films quality

(A) Photographs of the $EA_xCs_{1-x}PbI_3$ perovskite films.

(B–D) SEM images of $CsPbI_3$ (B), $EA_{0.1}Cs_{0.9}PbI_3$ (C), and $EA_{0.3}Cs_{0.7}PbI_3$ (D).

(E and F) XRD patterns (E) and Tauc plots (F) of the $EA_xCs_{1-x}PbI_3$ perovskite films.

diffraction peaks in the X-ray diffraction (XRD) patterns of these mixed mixed-cation $EA_xCs_{1-x}PbI_3$ perovskites could be attributed to the tetragonal perovskite phase (Wang et al., 2019a). The emerging diffraction peaks at 11.6° and 12.6° could be attributed to δ perovskite and PbI_2 (Akkerman et al., 2017), respectively, when EA content increased over 0.15, suggesting the deterioration of perovskites. No diffraction peaks related to EAI, PbI_2, or δ perovskite could be found in the XRD patterns of the $EA_{0.1}Cs_{0.9}PbI_3$ films, indicating the pure tetragonal perovskite phase. Tauc plots revealed that the band gaps of pure $CsPbI_3$ and $EA_{0.1}Cs_{0.9}PbI_3$ perovskites are 1.68 eV and 1.71 eV, respectively (Figure 2F).

Crystallization and intermediates

The effect of the addition of EAI on the perovskite crystallization was further investigated by UV-visible (UV-vis) and XRD measurements. The shape and the increased intensity of UV-vis spectrum of $CsPbI_3$ after annealing at 210°C for 1 min revealed the appearance of optical activity (Figure 3A). In contrast, $EA_{0.1}Cs_{0.9}PbI_3$ remained optically inactive after annealing for 1 min (Figure 3B). After annealing for 3 min, the UV-vis intensity of $CsPbI_3$ remains basically unchanged, whereas the intensity of $EA_{0.1}Cs_{0.9}PbI_3$ at 5 min was stronger than that at 3 min, indicative of the retarding crystallization of perovskite upon introducing EAI into precursor. The diffraction peak at 11.6° in XRD patterns of $EA_xCs_{1-x}PbI_3$ could be ascribed to $DMAPbI_3$ (Figures 3C and 3D). This characteristic peak of $DMAPbI_3$ can also be found in the XRD patterns of $EA_{0.1}Cs_{0.9}PbI_3$ and $CsPbI_3$ after annealing at 210°C for 2 min (Figure 3C and see Figure S3). The addition of dimethylammonium iodide (DMAI) in the precursor solution could form $DMAPbI_3$ intermediate. The relative ratio of $DMAPbI_3$/perovskite is very low after annealing at 210°C for 3 min providing the proof of the volatile additive of DMAI in the crystallization process (Pei et al., 2019; Bian et al., 2020). In experiment, we found that the introduction of EAI in the precursor solution could retard the crystallization of perovskite with a longer

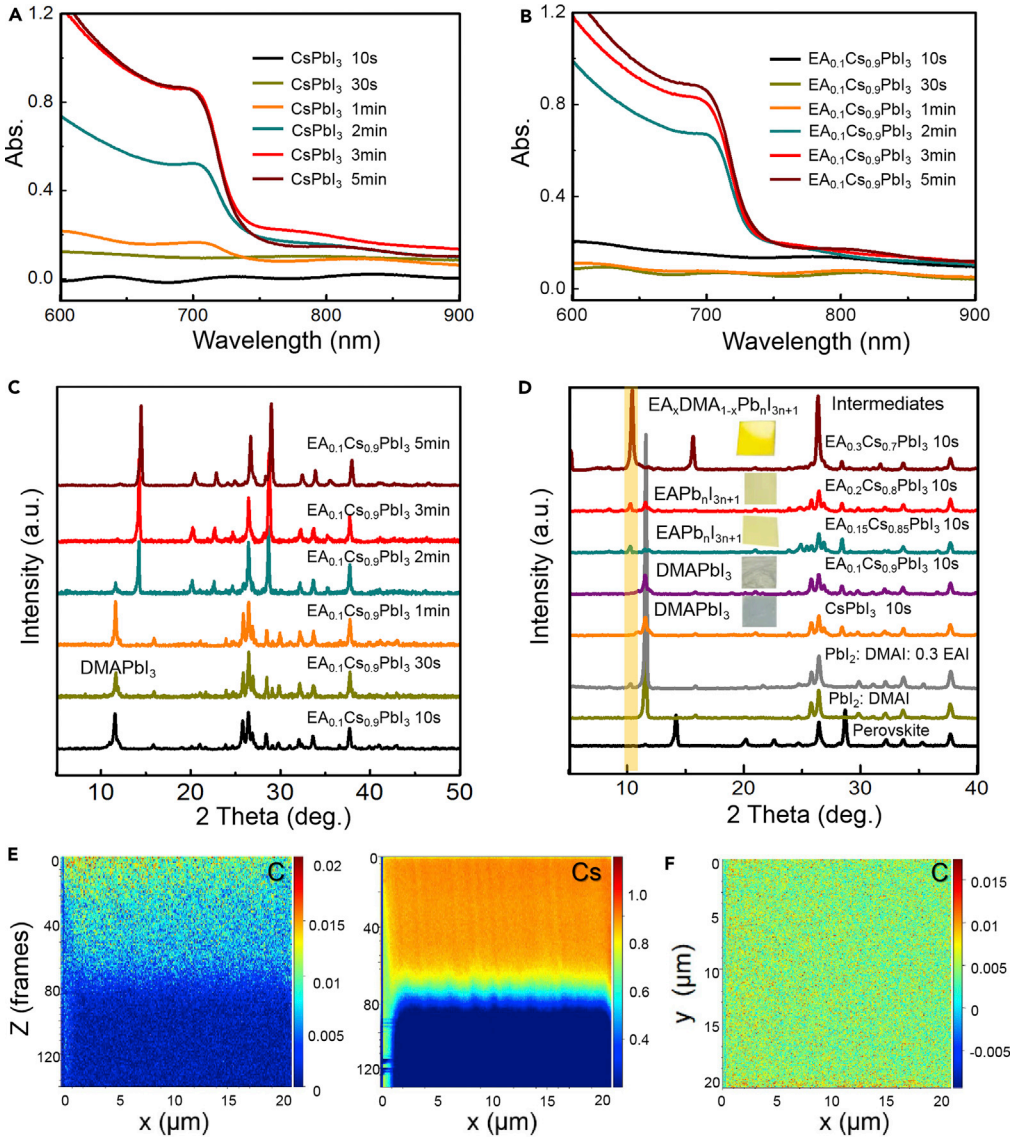

Figure 3. Crystallization and intermediates.

(A and B) UV spectra of $CsPbI_3$ (A) and $EA_{0.1}Cs_{0.9}PbI_3$ (B) at different annealing time.

(C and D) XRD patterns of $EA_{0.1}Cs_{0.9}PbI_3$ during different annealing time (C) and different $EA_xCs_{1-x}PbI_3$ intermediates annealing at 210°C for 10 s (D). The insets are the photographs of the corresponding intermediate films.

(E and F) Z-distribution mapping of C and Cs on $EA_{0.1}Cs_{0.9}PbI_3$ (E) and TOF-SIMS mapping of C (F).

annealing time to form the black phase (see Table S1). In particular, the film with EA fraction of 0.3 after annealing at 210°C for 10 s appeared orange. This orange intermediate film could be kept in dry air at room temperature for several days. XRD pattern of this orange intermediate showed distinct characteristic diffraction peaks at 10.3° and 15.7°. To further explore the effect of the addition of EAI on the intermediate phases, the precursors with PbI_2 + DMAI and PbI_2 + DMAI + EAI (Figure 3D) annealing at 210°C for 10 s were further characterized by XRD measurements. The emerging peak at 10.3° is induced by the addition of EAI. The color and the diffraction peaks of the orange intermediate film of $EA_{0.3}Cs_{0.7}PbI_3$ intermediate resemble the previously reported 2D $(CH_3(CH_2)_3NH_3)_2(MA)_2Pb_3I_{10}$ (Cao et al., 2015). Analysis by UV spectra further reveals the quasi-2D absorption nature of this intermediate film (Zhang et al., 2017) (see Figure S4). $EAPbI_3$ with a tolerance factor close to the upper limit had been previously reported to crystallize in a 2D structure with a large orthorhombic unit cell (Peng et al., 2017). XRD patterns of $EA_{0.1}Cs_{0.9}PbI_3$ and pure $CsPbI_3$ annealing at 210°C for 10 s revealed the presence of $DMAPbI_3$ intermediates (Figure 3D). For

$EA_{0.15}Cs_{0.85}PbI_3$ and $EA_{0.2}Cs_{0.8}PbI_3$, XRD patterns revealed the coexistence of $EAPb_nI_{3n+1}$ and $DMAPbI_3$ intermediates at the start of annealing. No characteristic diffraction peaks of $DMAPbI_3$ can be found in the XRD pattern of $EA_{0.3}Cs_{0.7}PbI_3$ intermediate film.

In low EA content, DMAI and PbI_2 first formed $DMAPbI_3$ intermediate. The sublimation of DMAI during the annealing process, concomitant with the incorporation of Cs^+ and EA^+ cations into the crystal lattice, generated the EA-Cs hybrid perovskite. When the EAI fractions increased to 0.15 and 0.2, EAI reacted with PbI_2 to form $EAPb_nI_{3n+1}$, alongside forming the $DMAPbI_3$ intermediate. Further sublimation of DMAI and transformation of $EAPb_nI_{3n+1}$ to perovskite was accompanied with Cs entering into the lattice. EAI with fractions over 0.3 would interact with DMAI to form quasi-2D intermediates, which then transformed into $EA_xCs_{1-x}PbI_3$ perovskites during the crystallization. The distribution of C and Cs throughout the $EA_{0.1}Cs_{0.9}PbI_3$ perovskite films prepared from $HPbI_{3+x}$-containing precursors was investigated using time-of-flight secondary ion mass spectrometry (TOF-SIMS). The depth profiles and the mapping images revealed that C was homogeneously distributed in the $EA_{0.1}Cs_{0.9}PbI_3$ perovskite film, indicating the successful incorporation of EA into $CsPbI_3$ (Figures 3E and 3F). Further analysis by the cross-sectional element profiling of the $EA_{0.1}Cs_{0.9}PbI_3$ revealed the homogeneous distribution of C and Cs (see Figure S5).

Photovoltaic performance and transport properties

$EA_xCs_{1-x}PbI_3$ perovskites were utilized as light harvesters for perovskite solar cells to evaluate the impact of alloyed EA on the photovoltaic performance of Cs-EA hybrid perovskites (Figure 4A). Overall, the PCE of $EA_xCs_{1-x}PbI_3$ perovskite solar cells was inversely proportional to the EA contents (Figure 4B). $EA_{0.1}Cs_{0.9}PbI_3$-based solar cell delivered a PCE of 16.01% with a V_{oc} of 1.026 V, a short-circuit current density (J_{sc}) of 20.21 mA cm^{-2}, and a fill factor (*FF*) of 77.20% (Figure 4B and see Table S2). The short-circuit current density of $EA_{0.1}Cs_{0.9}PbI_3$-based solar cell was slightly higher than that of pure $CsPbI_3$-based devices. With the increase of EA fractions from 0.1 to 0.3, the V_{oc} did not change considerably, whereas the J_{sc} and *FF* values declined greatly (Figures 4C and 4D). Further increase of EA content to 0.5 had a primary negative effect on the J_{sc}. The integrated current densities in typical external quantum efficiency (EQE) plots of the $EA_xCs_{1-x}PbI_3$ solar cells were close to the J_{sc} values obtained from the current density-voltage (*J-V*) measurements (Figure 4E). The carrier transit time of the EA-alloyed perovskites solar cells was investigated by the transient photocurrent decay (TPC) measurements (Figure 4F). TPC under short-circuit condition illustrates the photocarrier transit time across the bulk perovskite and the electrode interface (Ji et al., 2021; Zuo et al., 2017). The photocarrier transit time in pure $CsPbI_3$ was estimated to be ~2.7 μs, and little decrease was observed for $EA_{0.1}Cs_{0.9}PbI_3$ (~2.4 μs), indicating the enhanced charge transport in the $EA_{0.1}Cs_{0.9}PbI_3$-based devices. However, when EA fraction increased to 0.3, the transit time becomes longer (~3.5 μs), indicating an increased charge trap and reduced charge carrier lifetime in the $EA_{0.3}Cs_{0.7}PbI_3$-based devices. Space-charge limited current (SCLC) measurements were performed with an electron-only FTO/TiO_2/perovskite/phenyl-C61-butyric acid methyl ester (PCBM)/Ag device and utilized to estimate the charge trap densities (Figure 4G). In low applied voltages, a linear relationship of the current density and the bias voltage indicates an ohmic response. With the increase of the bias voltage, a kink point voltage could be observed in the SCLC plots reflecting a transition to the trap-filled limit (TFL) stage (Liu et al., 2017; Ji et al., 2017). The density of trap states (n_t) is proportional to V_{TFL} according to the equation (Bube, 1962): $V_{TFL} = en_tL^2/(2\varepsilon\varepsilon_0)$, where e is the elementary charge, n_t is the trap density, L is the thickness of the crystal between two Ag electrodes, ε is the relative dielectric constant of perovskite absorber (~5.3), and ε_0 is the dielectric constant of vacuum (Peng et al., 2017; Chen et al., 2020a). The measured V_{TFL} for the pristine $CsPbI_3$ film was ~0.35 V, whereas the value decreased to 0.24 V for $EA_{0.1}Cs_{0.9}PbI_3$. Accordingly, a decrease of n_t of ~3.0×10^{15} cm^{-3} for the $EA_{0.1}Cs_{0.9}PbI_3$-based devices was observed, compared with the control $CsPbI_3$ devices (4.5×10^{15} cm^{-3}), indicating the suppression of the non-radiative recombination in the $EA_{0.1}Cs_{0.9}PbI_3$-based devices. At higher voltage for the child region, the carrier mobility (μ) could be assessed with the equation: $I = 9\varepsilon\varepsilon_0 S\mu V^2/8L^3$, where S is the area of the electrodes and μ is the mobility (Chen et al., 2017; Chen and Wang, 2017). The electron mobility of $EA_{0.1}Cs_{0.9}PbI_3$ was higher than that of pure $CsPbI_3$. The dark current density of the $EA_{0.1}Cs_{0.9}PbI_3$-based devices was lower than that of the pure $CsPbI_3$-based devices by one order of magnitude (Figure 5A). The low leakage current density in $EA_{0.1}Cs_{0.9}PbI_3$-based devices suggested the suppressed charge recombination, which was further characterized by carrier transport measurements under illumination from electrochemical impedance spectroscopy (EIS) (Figure 5B). The middle frequency zone of EIS semicircle was closely associated with the interfacial recombination resistance between transport materials and perovskite (Chen et al., 2020c). Compared with $EA_{0.3}Cs_{0.7}PbI_3$ and pure $CsPbI_3$ devices, the $EA_{0.1}Cs_{0.9}PbI_3$-based

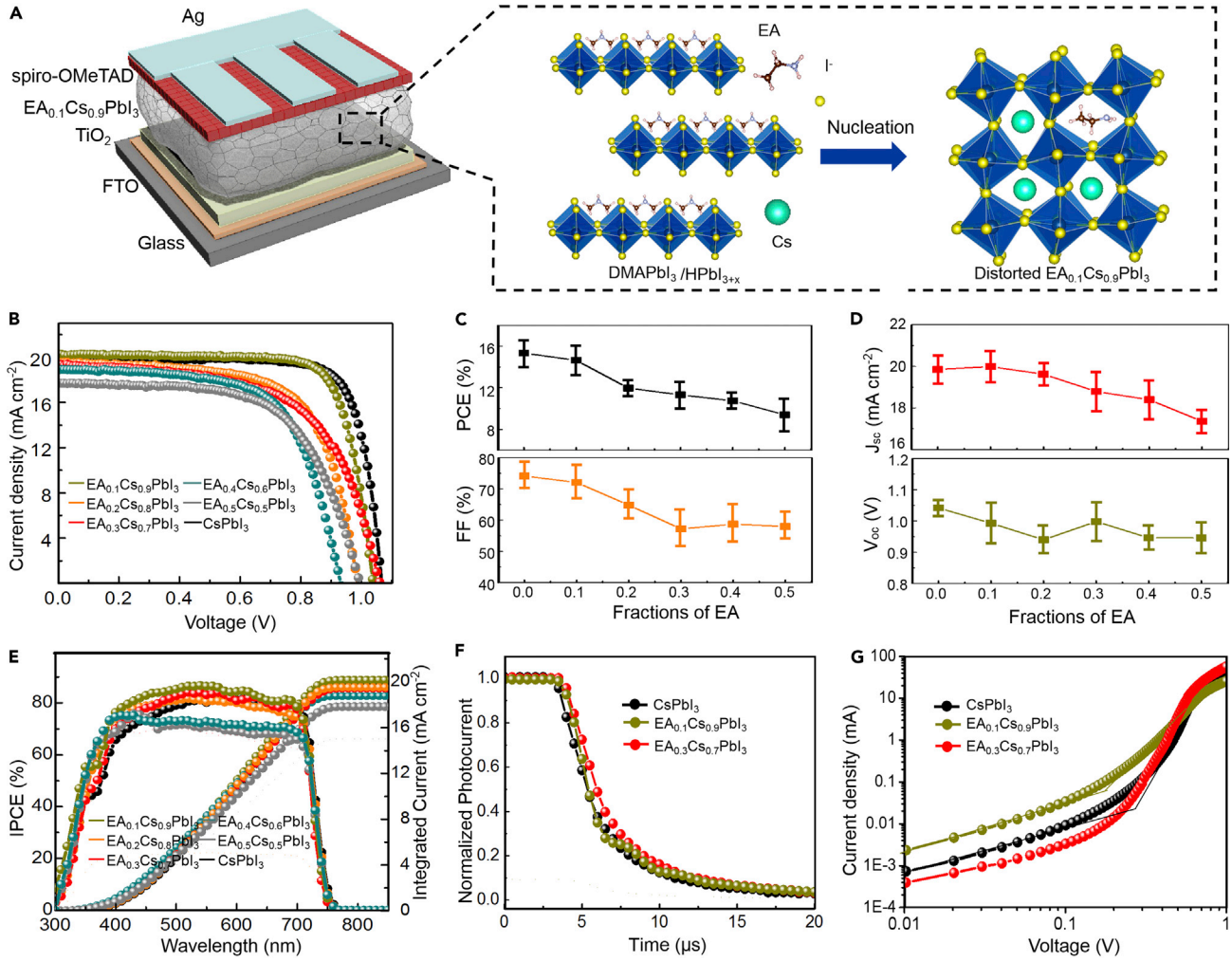

Figure 4. Photovoltaic performance

(A) Illustration of the $EA_xCs_{1-x}PbI_3$ perovskite solar cell.

(B–D) The selective best *J-V* performance of $EA_xCs_{1-x}PbI_3$-based devices under 1 sun measured by reverse scanning (B) and corresponding PCE, *FF* (C), and J_{sc}, V_{oc} (D).

(E and F) EQE spectra of $EA_xCs_{1-x}PbI_3$-based devices (E) and TPC plots of $CsPbI_3$, $EA_{0.1}Cs_{0.9}PbI_3$, and $EA_{0.3}Cs_{0.7}PbI_3$ (F).

(G) SCLC plots of electron-only FTO/TiO_2/$EA_xCs_{1-x}PbI_3$/PCBM/Ag.

devices had the largest impedance (largest circle arc), indicating a suppressed recombination in $EA_{0.1}Cs_{0.9}PbI_3$ (Zheng et al., 2018). The results reveal improved charge transport and suppressed charge recombination in $EA_{0.1}Cs_{0.9}PbI_3$ compared with $CsPbI_3$.

Conclusion

In summary, besides the generally used MA and FA organic cations to form hybrid perovskites, EA cation has been investigated for the first time as an alternative cation with which to fabricate hybrid perovskites by balancing lattice strain. Different from FA incorporation with distinct adsorption redshift, i.e., decrease of band gap, and the pure-phase FA-Cs mixed-cation perovskites at higher FA fractions, the EA incorporation would lead to a slight increase of the band gap, and a pure-phase EA-Cs hybrid perovskites could be obtained in a relatively small EA fraction ($x < 0.15$). The EA cation is presented as a potential replacement for Cs^+ in lead iodide perovskites, owing to the slightly increased band gap, enhanced phase stability, and improved transport properties of $EA_{0.1}Cs_{0.9}PbI_3$. The increased band gap was closely associated with a decrease of the average Pb-I-Pb angle. Meanwhile, the average Pb-I band distance was revealed to reflect the thermal stability of perovskites from DFT calculation. However, the incorporation of high fractions of EA

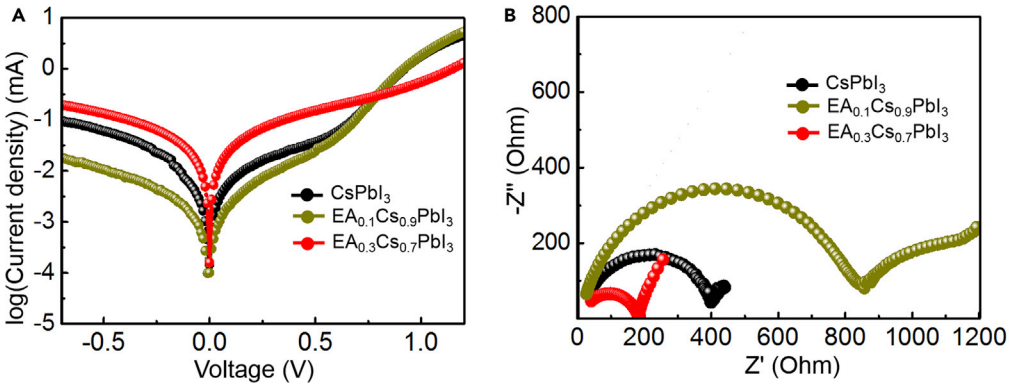

Figure 5. Transport properties

(A) *J-V* characteristics of $CsPbI_3$, $EA_{0.1}Cs_{0.9}PbI_3$, and $EA_{0.3}Cs_{0.7}PbI_3$ under dark.

(B) Nyquist plots of $CsPbI_3$, $EA_{0.1}Cs_{0.9}PbI_3$, and $EA_{0.3}Cs_{0.7}PbI_3$ under illumination of 50 mW cm^{-2}.

($x \geq 0.3$) would deteriorate the perovskite films with abundant pinholes and grain boundaries, which is unfavorable for the carrier's separation in solar cells owing to the nonradiative combination. Engineering large organic EA cations into $CsPbI_3$ perovskite is promising to tune the structure of $CsPbI_3$ perovskite with enhanced phase stability and transport properties for multijunction applications.

Limitations of the study

Here, a new A-site engineering approach based on structural distortion with different bond mixing is demonstrated to enlarge the band gap of $CsPbI_3$ from 1.68 eV to over 1.7 eV for potential multijunction application. Compared with traditional mixed halides engineering, this method can inherently eliminate the structural degradation of high-band-gap perovskites under illumination. The optimum amount of EA is revealed to be below 0.15 based on the pure phase of perovskite, structural stability, and transport property. $EA_{0.1}Cs_{0.9}PbI_3$ cannot reach the instant efficiency as high as $CsPbI_3$. However, the increase of the band gap of perovskite in the range of 1.7–1.8 eV will achieve the maximum efficiency of tandem solar cell. From 1.68 to 1.71 eV, the tandem solar cells' efficiency can improve ~4%. The light stability instead of thermal stability is revealed to reflect the instinct phase stability. It therefore demonstrates a proof-of-concept of applying structural distortion to improve the band gap and the structural stability of perovskite.

Resource availability

Lead contact

Further information and requests for resources should be directed to and will be fulfilled by the lead contact, Jun Chen (jun.chen@ucla.edu).

Materials availability

All chemicals were obtained from commercial resources and used as received.

Data and code availability

Data and all results are available on request from the authors. Calculated structure cif files can be found in https://doi.org/10.1016/j.isci.2021.102235.

METHODS

All methods can be found in the accompanying transparent methods supplemental file.

SUPPLEMENTAL INFORMATION

Supplemental information can be found online at https://doi.org/10.1016/j.isci.2021.102235.

ACKNOWLEDGMENTS

J.C. acknowledges the Henry Samueli School of Engineering and Applied Science and the Department of Bioengineering at University of California, Los Angeles, for the startup support. S.X. acknowledges the

support of the Initiative Postdocs Supporting Program (Grant No. BX20200209), China Postdoctoral Science Foundation (Grant No. 2020M671098), and the Alexander von Humboldt Research Fellowship. The authors thank Prof. Yixin Zhao for the assistance with the photovoltaic measurements.

AUTHOR CONTRIBUTIONS

J.C. designed and developed the concept and supervised the project. S.X. conducted the experiments, performed the analysis, and wrote the manuscript, and all authors discussed the results and commented on the manuscript.

DECLARATION OF INTERESTS

The authors declare no competing interests.

Received: January 21, 2021
Revised: February 9, 2021
Accepted: February 22, 2021
Published: March 19, 2021

REFERENCES

Akkerman, Q.A., Meggiolaro, D., Dang, Z., De Angelis, F., and Manna, L. (2017). Fluorescent alloy $CsPb_xMn_{1-x}I_3$ perovskite nanocrystals with high structural and optical stability. ACS Energy Lett. *2*, 2183–2186.

Aristidou, N., Sanchez-Molina, I., Chotchuangchutchaval, T., Brown, M., Martinez, L., Rath, T., and Haque, S.A. (2015). The role of oxygen in the degradation of methylammonium lead trihalide perovskite photoactive layers. Angew. Chem. Int. Ed. *127*, 8326–8330.

Bai, F., Zhang, J., Yuan, Y., Liu, H., Li, X., Chueh, C.-C., Yan, H., Zhu, Z., and Jen, A.K.Y. (2019). A 0D/3D heterostructured all-inorganic halide perovskite solar cell with high performance and enhanced phase stability. Adv. Mater. *31*, 1904735.

Beal, R.E., Hagström, N.Z., Barrier, J., Gold-Parker, A., Prasanna, R., Bush, K.A., Passarello, D., Schelhas, L.T., Brüning, K., and Tassone, C.J. (2020). Structural origins of light-induced phase segregation in organic-inorganic halide perovskite photovoltaic materials. Matter *2*, 207–219.

Bian, H., Wang, H., Li, Z., Zhou, F., Xu, Y., Zhang, H., Wang, Q., Ding, L., Liu, S., and Jin, Z. (2020). Unveiling the effects of hydrolysis-derived DMAI/$DMAPbI_x$ intermediate compound on the performance of $CsPbI_3$ Solar Cells. Adv. Sci. *77*, 1902868.

Binek, A., Hanusch, F.C., Docampo, P., and Bein, T. (2015). Stabilization of the trigonal high-temperature phase of formamidinium lead iodide. J. Phys. Chem. Lett. *6*, 1249–1253.

Bischak, C.G., Hetherington, C.L., Wu, H., Aloni, S., Ogletree, D.F., Limmer, D.T., and Ginsberg, N.S. (2017). Origin of reversible photoinduced phase separation in hybrid perovskites. Nano Lett. *17*, 1028–1033.

Bube, R.H. (1962). Trap density determination by space-charge-limited currents. J. Appl. Phys. *33*, 1733–1737.

Cao, D.H., Stoumpos, C.C., Farha, O.K., Hupp, J.T., and Kanatzidis, M.G. (2015). 2D Homologous perovskites as light-absorbing materials for solar cell applications. J. Am. Chem. Soc. *137*, 7843–7850.

Chen, G., Li, Y., Bick, M., and Chen, J. (2020a). Smart textiles for electricity generation. Chem. Rev. *120*, 3668–3720.

Chen, H., Fu, W., Huang, C., Zhang, Z., Li, S., Ding, F., Shi, M., Li, C.Z., Jen, A.K.Y., and Chen, H. (2017). Molecular engineered hole-extraction materials to enable dopant-free, efficient p-i-n perovskite solar cells. Adv. Energy Mater. *7*, 1700012.

Chen, J., and Wang, Z.L. (2017). Reviving vibration energy harvesting and self-powered sensing by a triboelectric nanogenerator. Joule *1*, 480–521.

Chen, J., Huang, Y., Zhang, N., Zou, H., Liu, R., Tao, C., Fan, X., and Wang, Z.L. (2016). Micro-cable structured textile for simultaneously harvesting solar and mechanical energy. Nat. Energy *1*, 16138.

Chen, S., Zhang, Y., Zhang, X., Zhao, J., Zhao, Z., Su, X., Hua, Z., Zhang, J., Cao, J., Feng, J., et al. (2020b). General decomposition pathway of organic-inorganic hybrid perovskites through an intermediate superstructure and its suppression mechanism. Adv. Mater. *32*, 2001107.

Chen, Y., Yang, J., Wang, S., Wu, Y., Yuan, N., and Zhang, W.-H. (2020c). Interfacial contact passivation for efficient and stable cesium-formamidinium double-cation lead halide perovskite solar cells. iScience *23*, 100762.

Chen, Y., Zhao, L., Peng, L., Li, X., Zheng, K., Qu, J., and Song, J. (2019). Solution-phase synthesis of $CsPbI_3$ nanowire clusters via polymer-induced anisotropic growth and self-assembly. Chem. Commun. *55*, 8266–8269.

Deng, J., Li, J., Yang, Z., and Wang, M. (2019). All-inorganic lead halide perovskites: a promising choice for photovoltaics and detectors. J. Mater. Chem. C *7*, 12415–12440.

Egger, A.T., Hörmann, L., Jeindl, A., Scherbela, M., Obersteiner, V., Todorović, M., Rinke, P., and Hofmann, O.T. (2020). Charge transfer into organic thin films: a deeper insight through machine-learning-assisted structure search. Adv. Sci. *7*, 2000992.

Ghosh, T., Aharon, S., Shpatz, A., Etgar, L., and Ruhman, S. (2018). Reflectivity effects on pump-probe spectra of lead halide perovskites: comparing thin films versus nanocrystals. ACS Nano *12*, 5719–5725.

Hazarika, A., Zhao, Q., Gaulding, E.A., Christians, J.A., Dou, B., Marshall, A.R., Moot, T., Berry, J.J., Johnson, J.C., and Luther, J.M. (2018). Perovskite quantum dot photovoltaic materials beyond the reach of thin films: full-range tuning of A-site cation composition. ACS Nano *12*, 10327–10337.

Hoke, E.T., Slotcavage, D.J., Dohner, E.R., Bowring, A.R., Karunadasa, H.I., and McGehee, M.D. (2015). Reversible photo-induced trap formation in mixed-halide hybrid perovskites for photovoltaics. Chem. Sci. *6*, 613–617.

Hsu, H.-L., Chang, C.-C., Chen, C.-P., Jiang, B.-H., Jeng, R.-J., and Cheng, C.-H. (2015). High-performance and high-durability perovskite photovoltaic devices prepared using ethylammonium iodide as an additive. J. Mater. Chem. A *3*, 9271–9277.

Jeong, B., Han, H., Kim, H.H., Choi, W.K., Park, Y.J., and Park, C. (2020). Polymer-assisted nanoimprinting for environment-and phase-stable perovskite nanopatterns. ACS Nano *14*, 1645–1655.

Ji, F., Pang, S., Zhang, L., Zong, Y., Cui, G., Padture, N.P., and Zhou, Y. (2017). Simultaneous evolution of uniaxially oriented grains and ultralow-density grain-boundary network in $CH_3NH_3PbI_3$ perovskite thin films mediated by precursor phase metastability. ACS Energy Lett. *2*, 2727–2733.

Ji, J., Perepichka, L.F., Bai, J., Hu, D., Xu, X., Liu, M., Wang, T., Zhao, C., Meng, H., and Huang, W. (2021). Three-phase elecric power driven electoluminescent devices. Nat. Commun. *12*, 54.

Juarez-Perez, E.J., Hawash, Z., Raga, S.R., Ono, L.K., and Qi, Y. (2016). Thermal degradation of CH_3 NH_3PbI_3 perovskite into NH_3 and CH_3I gases

observed by coupled thermogravimetry-mass spectrometry analysis. Energy Environ. Sci. *9*, 3406–3410.

Lau, C.F.J., Wang, Z., Sakai, N., Zheng, J., Liao, C.H., Green, M., Huang, S., Snaith, H.J., and Ho-Baillie, A. (2019). Fabrication of efficient and stable $CsPbI_3$ perovskite solar cells through cation exchange process. Adv. Energy Mater. *9*, 1901685.

Lee, J.-W., Seo, S., Nandi, P., Jung, H.S., Park, N.-G., and Shin, H. (2021). Dynamic structural property of organic-inorganic metal halide perovskite. iScience *24*, 101959.

Li, B., Zhang, Y., Fu, L., Yu, T., Zhou, S., Zhang, L., and Yin, L. (2018a). Surface passivation engineering strategy to fully-inorganic cubic $CsPbI_3$ perovskites for high-performance solar cells. Nat. Commun. *9*, 1076.

Li, J., Järvi, J., and Rinke, P. (2018b). Multiscale model for disordered hybrid perovskites: the concept of organic cation pair modes. Phys. Rev. B *98*, 045201.

Li, Y., Shi, J., Zheng, J., Bing, J., Yuan, J., Cho, Y., Tang, S., Zhang, M., Yao, Y., Lau, C.F.J., et al. (2020a). Acetic acid assisted crystallization strategy for high efficiency and long-term stable perovskite solar cell. Adv. Sci. *7*, 1903368.

Li, Z., Zhou, F., Wang, Q., Ding, L., and Jin, Z. (2020b). Approaches for thermodynamically stabilized $CsPbI_3$ solar cells. Nano Energy *71*, 104634.

Lin, Y.-H., Sakai, N., Da, P., Wu, J., Sansom, H.C., Ramadan, A.J., Mahesh, S., Liu, J., Oliver, R.D., and Lim, J. (2020). A piperidinium salt stabilizes efficient metal-halide perovskite solar cells. Science *369*, 96–102.

Liu, D., Yang, C., Bates, M., and Lunt, R.R. (2018). Room temperature processing of inorganic perovskite films to enable flexible solar cells. iScience *6*, 272–279.

Liu, Z., Hu, J., Jiao, H., Li, L., Zheng, G., Chen, Y., Huang, Y., Zhang, Q., Shen, C., and Chen, Q. (2017). Chemical reduction of intrinsic defects in thicker heterojunction planar perovskite solar cells. Adv. Mater. *29*, 1606774.

Longo, G., Momblona, C., La-Placa, M.-G., Gil-Escrig, L.N., Sessolo, M., and Bolink, H.J. (2017). Fully vacuum-processed wide band gap mixed-halide perovskite solar cells. ACS Energy Lett. *3*, 214–219.

Lu, H., Krishna, A., Zakeeruddin, S.M., Grzel, M., and Hagfeldt, A. (2020). Compositional and interface engineering of organic-inorganic lead halide perovskite solar cells. iScience *23*, 101359.

Marronnier, A., Roma, G., Boyer-Richard, S., Pedesseau, L., Jancu, J.-M., Bonnassieux, Y., Katan, C., Stoumpos, C.C., Kanatzidis, M.G., and Even, J. (2018). Anharmonicity and disorder in the black phases of cesium lead iodide used for stable inorganic perovskite solar cells. ACS Nano *12*, 3477–3486.

Mauck, C.M., and Tisdale, W.A. (2019). Excitons in 2D organic-inorganic halide perovskites. Trends Chem. *1*, 380–393.

Miyazawa, Y., Ikegami, M., Chen, H.-W., Ohshima, T., Imaizumi, M., Hirose, K., and Miyasaka, T. (2018). Tolerance of perovskite solar cell to high-energy particle irradiations in space environment. iScience *2*, 148–155.

Nenon, D.P., Pressler, K., Kang, J., Koscher, B.A., Olshansky, J.H., Osowiecki, W.T., Koc, M.A., Wang, L.-W., and Alivisatos, A.P. (2018). Design principles for trap-free $CsPbX_3$ nanocrystals: enumerating and eliminating surface halide vacancies with softer lewis bases. J. Am. Chem. Soc. *140*, 17760–17772.

Pei, Y., Liu, Y., Li, F., Bai, S., Jian, X., and Liu, M. (2019). Unveiling property of hydrolysis-derived $DMAPbI_3$ for perovskite devices: composition engineering, defect mitigation, and stability optimization. iScience *15*, 165–172.

Peng, J., Wu, Y., Ye, W., Jacobs, D.A., Shen, H., Fu, X., Wan, Y., Wu, N., Barugkin, C., and Nguyen, H.T. (2017). Interface passivation using ultrathin polymer-fullerene films for high-efficiency perovskite solar cells with negligible hysteresis. Energy Environ. Sci. *10*, 1792–1800.

Qing, J., Kuang, C., Wang, H., Wang, Y., Liu, X.-K., Bai, S., Li, M., Sum, T.C., Hu, Z., Zhang, W., et al. (2019). High-quality ruddlesden-popper perovskite films based on in situ formed organic spacer cations. Adv. Mater. *31*, 1703852.

Ripalda, J.M., Chemisana, D., Llorens, J.M., and Garca, I. (2020). Location-specific spectral and thermal effects in tracking and fixed tilt photovoltaic systems. iScience *23*, 101634.

Sadeghi, S., Jalali, H.B., Srivastava, S.B., Melikov, R., Baylam, I., Sennaroglu, A., and Nizamoglu, S. (2020). High-performance, large-area, and ecofriendly luminescent solar concentrators using copper-doped InP quantum dots. iScience *23*, 101272.

Stoumpos, C.C., Malliakas, C.D., and Kanatzidis, M.G. (2013). Semiconducting tin and lead iodide perovskites with organic cations: phase transitions, high mobilities, and near-infrared photoluminescent properties. Inorg. Chem. *52*, 9019–9038.

Straus, D.B., Guo, S., Abeykoon, A.M.M., and Cava, R.J. (2020). Understanding the instability of the halide perovskite $CsPbI_3$ through temperature-dependent structural analysis. Adv. Mater. *32*, 2001069.

Tian, J., Wang, J., Xue, Q., Niu, T., Yan, L., Zhu, Z., Li, N., Brabec, C.J., Yip, H.L., and Cao, Y. (2020). Composition engineering of all-inorganic perovskite film for efficient and operationally stable solar cells. Adv. Funct. Mater. *30*, 2001764.

Tian, J., Xue, Q., Tang, X., Chen, Y., Li, N., Hu, Z., Shi, T., Wang, X., Huang, F., Brabec, C.J., et al. (2019). Dual interfacial design for efficient $CsPbI_2Br$ perovskite solar cells with improved photostability. Adv. Mater. *31*, 1901152.

Wang, B., and Chen, T. (2016). Exceptionally stable $CH_3NH_3PbI_3$ films in moderate humid environmental condition. Adv. Sci. *3*, 2198.

Wang, K., Jin, Z., Liang, L., Bian, H., Bai, D., Wang, H., Zhang, J., Wang, Q., and Liu, S. (2018). All-inorganic cesium lead iodide perovskite solar cells with stabilized efficiency beyond 15%. Nat. Commun. *9*, 1–8.

Wang, Y., Dar, M.I., Ono, L.K., Zhang, T., Kan, M., Li, Y., Zhang, L., Wang, X., Yang, Y., and Gao, X. (2019a). Thermodynamically stabilized β-$CsPbI_3$-based perovskite solar cells with efficiencies>18%. Science *365*, 591–595.

Wang, Y., Liu, X., Zhang, T., Wang, X., Kan, M., Shi, J., and Zhao, Y. (2019b). The role of dimethylammonium iodide in $CsPbI_3$ perovskite fabrication: additive or dopant? Angew. Chem. Int. Ed. *58*, 16691–16696.

Wang, Z., Song, Z., Yan, Y., Liu, S., and Yang, D. (2019c). Perovskite-a perfect top cell for tandem devices to break the S-Q limit. Adv. Sci. *6*, 1801704.

Wheeler, L.M., Sanehira, E.M., Marshall, A.R., Schulz, P., Suri, M., Anderson, N.C., Christians, J.A., Nordlund, D., Sokaras, D., and Kroll, T. (2018). Targeted ligand-exchange chemistry on cesium lead halide perovskite quantum dots for high-efficiency photovoltaics. J. Am. Chem. Soc. *140*, 10504–10513.

Wu, T., Wang, Y., Dai, Z., Cui, D., Wang, T., Meng, X., Bi, E., Yang, X., and Han, L. (2019). Efficient and stable $CsPbI_3$ solar cells via regulating lattice distortion with surface organic terminal groups. Adv. Mater. *31*, 1900605.

Xu, F., Zhang, T., Li, G., and Zhao, Y. (2017). Mixed cation hybrid lead halide perovskites with enhanced performance and stability. J. Mater. Chem. A *5*, 11450–11461.

Xu, N., Li, Y., Ricciarelli, D., Wang, J., Mosconi, E., Yuan, Y., Deangelis, F., Zakeeruddin, S.M., Grtzel, M., and Wang, P. (2019). An Oxa[5] helicene-based racemic semiconducting glassy film for photothermally stable perovskite solar cells. iScience *15*, 234–242.

Yang, T.C.-J., Fiala, P., Jeangros, Q., and Ballif, C. (2018). High-bandgap perovskite materials for multijunction solar cells. Joule *2*, 1421–1436.

Yang, W., Zhong, D., Shi, M., Qu, S., and Chen, H. (2019). Toward highly thermal stable perovskite solar cells by rational design of interfacial layer. iScience *22*, 534–543.

Yi, C., Luo, J., Meloni, S., Boziki, A., Ashari-Astani, N., Grätzel, C., Zakeeruddin, S.M., Röthlisberger, U., and Grätzel, M. (2016). Entropic stabilization of mixed A-cation ABX_3 metal halide perovskites for high performance perovskite solar cells. Energy Environ. Sci. *9*, 656–662.

Yu, Z.J., Leilaeioun, M., and Holman, Z. (2016). Selecting tandem partners for silicon solar cells. Nat. Energy *1*, 16137.

Zhang, J., Liu, W., Zhang, M., Liu, Y., Zhou, G., Xu, S., Zhang, F., Zhu, H., Liu, F., and Zhu, X. (2019). Revealing the critical role of the HOMO alignment on maximizing current extraction and suppressing energy loss in organic solar cells. iScience *19*, 883–893.

Zhang, N., Chen, J., Huang, Y., Guo, W., Yang, J., Du, J., Fan, X., and Tao, C. (2016). A wearable all-solid photovoltaic textile. Adv. Mater. *28*, 263.

Zhang, N., Huang, F., Zhao, S., Lv, X., Zhou, Y., Xiang, S., Xu, S., Li, Y., Chen, G., Tao, C., et al. (2020). Photo-rechargeable fabrics as sustainable and robust power sources for wearable bioelectronics. Matter *2*, 1260–1269.

Zhang, T., Dar, M.I., Li, G., Xu, F., Guo, N., Gratzel, M., and Zhao, Y. (2017). Bication lead iodide 2D perovskite component to stabilize inorganic alpha-$CsPbI_3$ perovskite phase for high-efficiency solar cells. Sci. Adv. *3*, e1700841.

Zheng, G., Zhu, C., Ma, J., Zhang, X., Tang, G., Li, R., Chen, Y., Li, L., Hu, J., and Hong, J. (2018). Manipulation of facet orientation in hybrid perovskite polycrystalline films by cation cascade. Nat. Commun. *9*, 2793.

Zheng, L., Cheng, G., Chen, J., Lin, L., Wang, J., Liu, Y., and Wang, Z.L. (2015). A hybridized power panel to simultaneously generate electricity from sunlight, raindrops and wind around the clock. Adv. Energy Mater. *5*, 1501152.

Zuo, L., Guo, H., Quilettes, D.W., Jariwala, S., De Marco, N., Dong, S., DeBlock, R., Ginger, D.S., Dunn, B., Wang, M., et al. (2017). Polymer-modified halide perovskite films for efficient and stable planar heterojunction solar cells. Sci. Adv. *3*, e1700106.

iScience, Volume *24*

Supplemental information

Engineering bandgap of $CsPbI_3$ over 1.7 eV with enhanced stability and transport properties

Shumao Xu, Alberto Libanori, Gan Luo, and Jun Chen

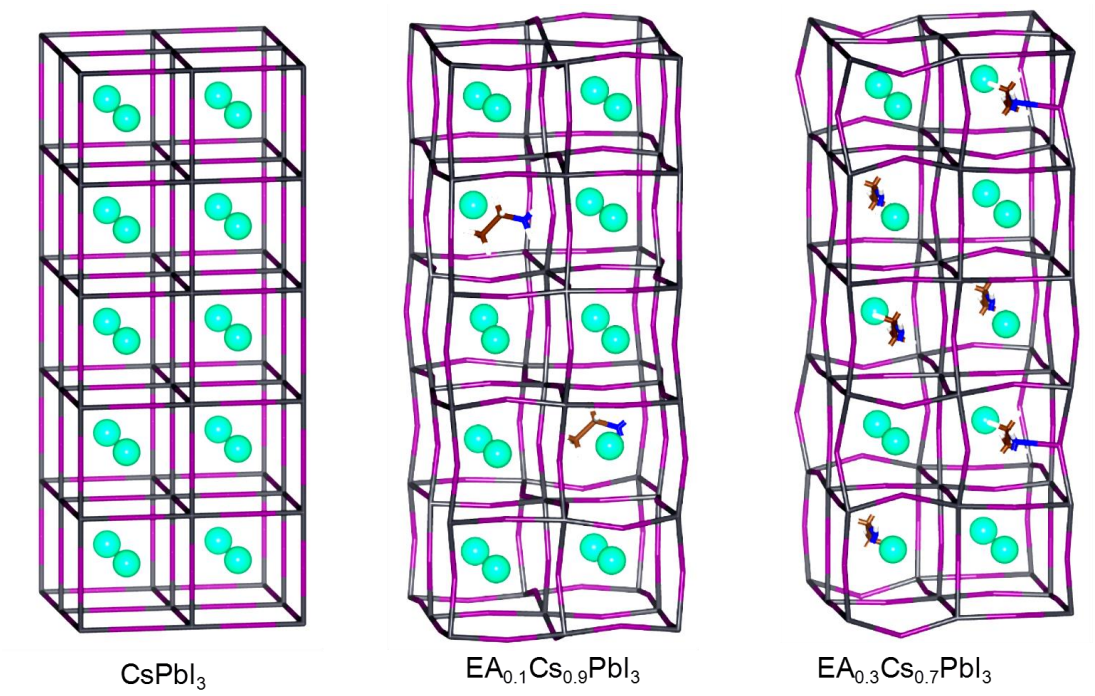

Figure S1. Crystal structure of $CsPbI_3$, $EA_{0.1}Cs_{0.9}PbI_3$ and $EA_{0.3}Cs_{0.7}PbI_3$. **Related to Figure 1.**

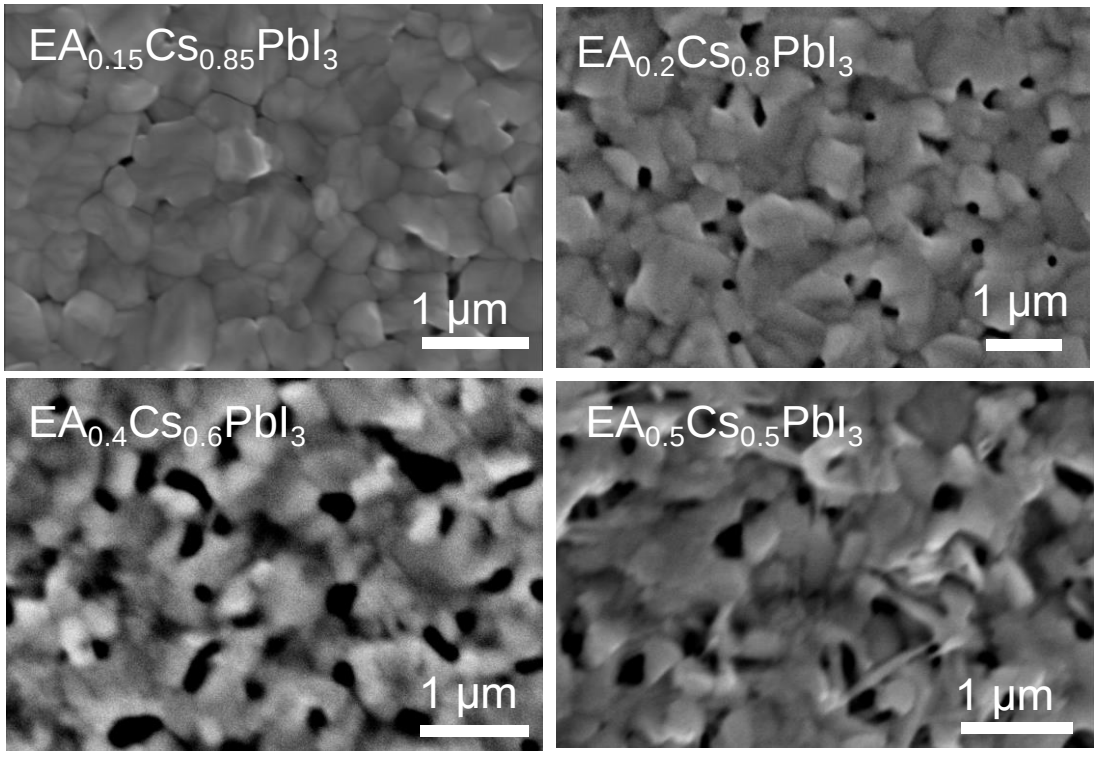

Figure S2. SEM images of $EA_{0.15}Cs_{0.85}PbI_3$, $EA_{0.2}Cs_{0.8}PbI_3$, $EA_{0.4}Cs_{0.6}PbI_3$ and $EA_{0.5}Cs_{0.5}PbI_3$. **Related to Figure 2.**

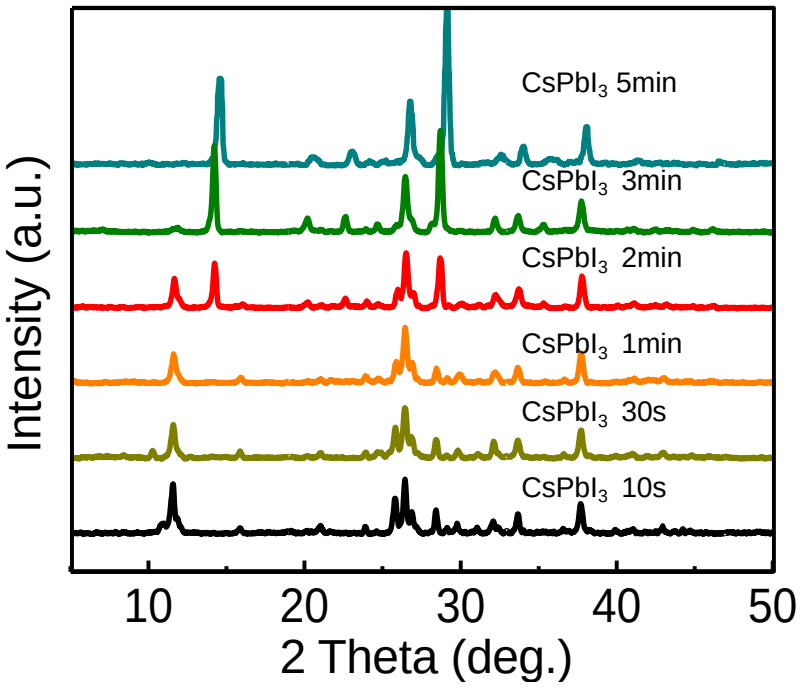

Figure S3. XRD patterns of $CsPbI_3$ perovskites after annealing at 210 °C for different time. **Related to Figure 3.**

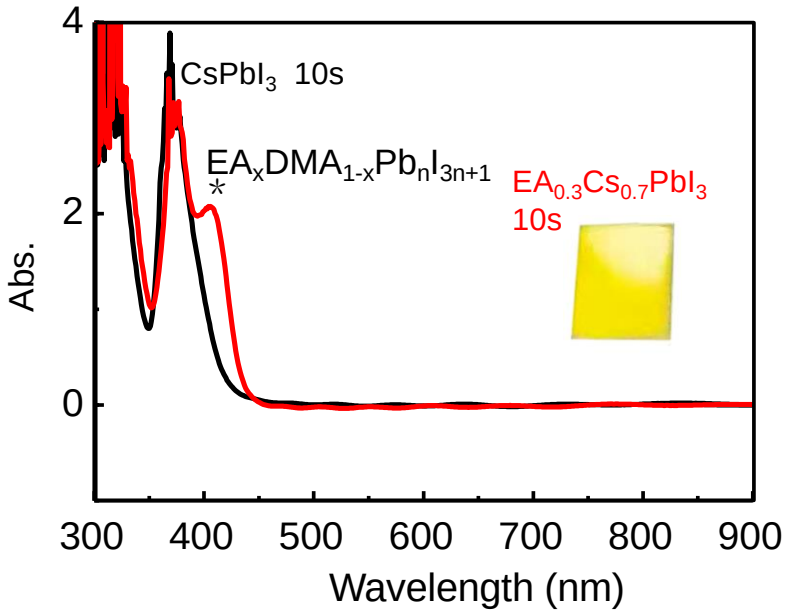

Figure S4. UV-spectra of the $EA_{0.3}Cs_{0.7}PbI_3$ and $CsPbI_3$ intermediates annealing at 210 °C for 10 s.

Related to Figure 3.

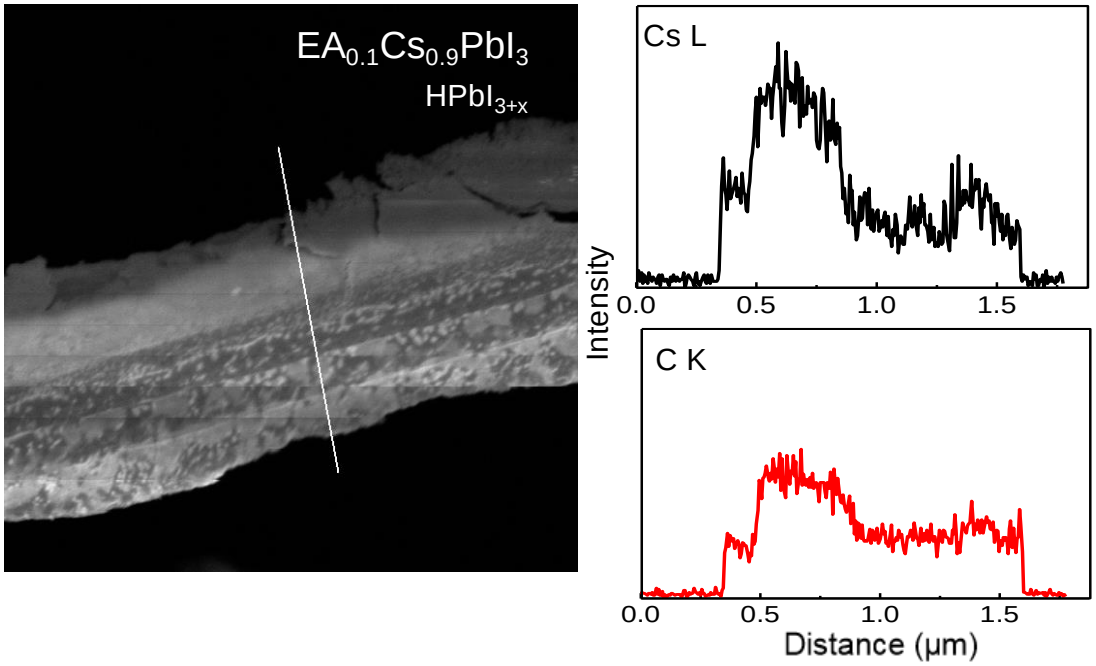

Figure S5. Cross-sectional SEM image and EDS line scanning of $EA_{0.1}Cs_{0.9}PbI_3$. **Related to Figure 3.**

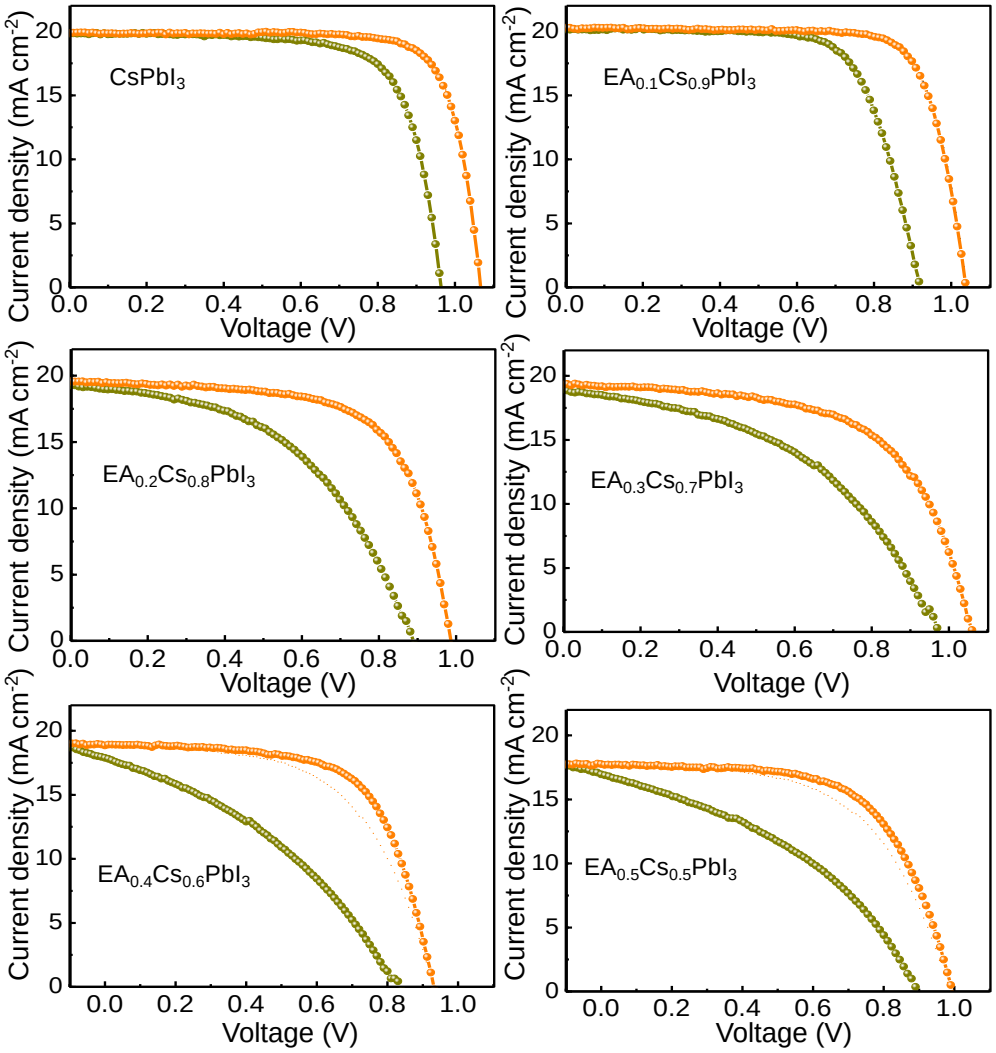

Figure S6. *J-V* characteristics of $EA_xCs_{1-x}PbI_3$ based device under simulated AM 1.5 G solar illumination of 100 mW cm^{-2} in reverse and forward scans. **Related to Figure 4.**

Supplemental Tables

Table S1. The recorded annealing time for $EA_xCs_{1-x}PbI_3$ during crystallization. **Related to Figure 3.**

	Crystallization beginning (Black phase emerging)	Complete crystallization (Black film)	Glossy Film	Turning Yellow
$CsPbI_3$	~80 s	120 s		
$EA_{0.1}Cs_{0.9}PbI_3$	94 s	161 s	218 s	
$EA_{0.2}Cs_{0.8}PbI_3$	109 s	173 s	228 s	
$EA_{0.3}Cs_{0.7}PbI_3$	120 s	240 s	378 s	557 s
$EA_{0.4}Cs_{0.6}PbI_3$, $EA_{0.5}Cs_{0.5}PbI_3$	150 s	378 s		

Table S2. Photovoltaic parameters of $EA_xCs_{1-x}PbI_3$ solar cells under 1 sun (AM 1.5 illumination). **Related to Figure 4.**

	PCE (%)	*FF*	*J*sc (mA cm^{-2})	*V*oc (V)
$CsPbI_3$	16.649	0.785	19.876	1.067
$EA_{0.1}Cs_{0.9}PbI_3$	16.008	0.772	20.206	1.026
$EA_{0.2}Cs_{0.8}PbI_3$	12.760	0.661	19.575	0.987
$EA_{0.3}Cs_{0.7}PbI_3$	12.610	0.641	19.479	1.009
$EA_{0.4}Cs_{0.6}PbI_3$	11.385	0.648	18.852	0.932
$EA_{0.5}Cs_{0.5}PbI_3$	10.995	0.623	17.753	0.994

Transparent Methods

Materials and Chemicals.

CsI and PbI_2 were purchased from Alfa Aesar. Dimethylammonium iodine (DMAI) were purchased from *J&K* Ltd. Ethylamine iodine (EAI), anhydrous dimethylformamide (DMF) and bis(trifluoromethane) sulfonamide lithium salt (LiTFSI) were purchased from Sigma-Aldrich. 4-tert-butylpyridine (TBP) was purchased from TCL Co., Ltd.

Device Fabrication.

A compact TiO_2 layer was deposited on the laser patterned FTO substrate by spraying pyrolysis of 0.2 M Ti^{IV} bis(ethyl acetoacetate)-diisopropoxide in butanol solution at 450 °C, and then annealed at 450 °C for 1 h. 0.7 M $EA_xCs_{1-x}PbI_3$ perovskite precursor was prepared by dissolving stoichiometric EAI, CsI, PbI_2 and DMAI with *x*: 1-*x*: 1: 1.2 molar ratio in DMF (*x* = 0.1-0.5). 0.6 M $EA_xCs_{1-x}PbI_3$ perovskite precursor was prepared by dissolving stoichiometric EAI, CsI and $HPbI_{3+x}$ with *x*: 1-*x*: 1 molar ratio in DMF (*x* = 0.1-0.5). Then, the $CsPbI_3$ active layer was spin-coated on the pre-warmed TiO_2/FTO substrate at 70 °C (3000 rpm, 30 s). Further annealing the substrates at 210 °C for 6 min fabricated the $EA_xCs_{1-x}PbI_3$ perovskite films. The devices were assembled in a dry box (10~20% RH). A layer of hole transport material (HTM) composed of 0.1 M spiro-MeOTAD, 0.035 M bis(trifluoromethane) sulfonamide lithium salt (LiTFSI), and 0.12 M 4-tert-butylpyridine (TBP) in chlorobenzene/acetonitrile (10:1, *v*/*v*) solution was spin-coated onto top of the above annealed films at 4000 rpm for 25 s. Finally, thermal evaporation was utilized to deposit a 100-nm thick Ag layer at the evaporation rate of ~0.2 Å s^{-1} from 0-300 Å, and ~0.6 Å s^{-1} from 300-1000 Å. All the process for the metal evaporation was processed in N_2 atmosphere with < 10% R.H.

Characterization and Measurements.

UV-vis spectra were detected by a spectrophotometer (DR6000 HACH, USA). XRD patterns were performed on Shimadzu XRD-6100 diffractometer with Cu Kα radiation for crystal structural characterization. The morphology of the films was assessed using a FESEM (FEI NOVA Nano SEM 230, USA). TOF-SIMS and TOF-SEM were carried out on a TESCAN Gaia3 FESEM. The *J*-*V* characteristics were measured with a Keithley 2401 source meter at a scan rate of 0.05 V s^{-1} under a simulated AM 1.5 G illumination (100 mW cm^{-2}) using Enlitech's 3A light source. EQE was measured on a QE-3011 system (Enlitech). The TPC measurements were carried out by a microsecond pulse of a white light incident on solar cells under short circuit conditions with a very

low resistor at 20 Ω in the dark.

DFT Calculations.

First-principles electronic structure calculations were carried out using the Vienna ab initio simulation package (VASP) code[1,2] within the generalized gradient approximation (GGA) approach[3]. The generalized gradient approximation (GGA) with the Perdew-Burke-Ernzerhof (PBE) functional was used to describe the electronic exchange and correlation effects. Uniform G-centered k-points meshes with a resolution of $2\pi \times 0.04$ $Å^{-1}$ and Methfessel-Paxton electronic smearing were adopted for the integration in the Brillouin zone for geometric optimization. The simulation was run with a cutoff energy of 500 eV throughout the computations. These settings ensured convergence of the total energies to within 1 meV per atom. Structure relaxation proceeded until all forces on atoms were less than 1 meV $Å^{-1}$ and the total stress tensor was within 0.01 GPa of the target value. The simulation cells were adopted by supercells of $CsPbI_3$, *i.e.*, $Cs_{20}Pb_{20}I_{60}$, $EA_2Cs_{18}Pb_{20}I_{60}$. In order to keep the temperature and volume constant, we used the NVT ensemble during the MD simulation and the Nosé-Hoover thermostat was used in the NVT ensemble to keep the temperature. The melting process was calculated by MD simulation of the movements of the Cs, Pb, I, C, N and H atoms with 2000 steps (3 fp s^{-1}).

Supplemental References

1. Kresse, G., and Furthmüller, J. (1996). Efficient iterative schemes for ab initio total-energy calculations using a plane-wave basis set. Phys. Rev. B *54*, 11169.

2. Kresse, G., and Furthmüller, J. (1996). Efficiency of ab-initio total energy calculations for metals and semiconductors using a plane-wave basis set. Comput. Mater. Sci. *6*, 15-50.

3. Perdew, J.P., Burke, K., and Ernzerhof, M. (1996). Generalized gradient approximation made simple. Phys. Rev. Lett. *77*, 3865.